

Thermal Inertia of Conductivity Cells: Observations with a Sea-Bird Cell

ROLF G. LUECK* AND JAMES J. PICKLO

Johns Hopkins University, Chesapeake Bay Institute, Baltimore

(Manuscript received 19 December 1989, in final form 23 May 1990)

ABSTRACT

We have examined the magnitude and relaxation time of the thermal anomaly of the fluid flowing through the conductivity cell manufactured by Sea-Bird Electronics (SBE) that is induced by the heat stored in the wall of this cell using oceanic data collected in a thermohaline staircase. The relaxation is 9 to 10 s, about twice the value predicted by Lueck, while the initial magnitude of the conductivity error is 2.8%, about 35% smaller than predicted. The error in the measured conductivity is significant and long-lived and results in density errors detectable for 45 s after the sensor enters an isopycnal layer. An efficient numerical algorithm removes the anomaly from the measured conductivity signal and clears the resulting error from the computed salinity and density.

1. Introduction

The theoretical thermal model of a hollow circular cylinder by Lueck (1990, hereafter RGL) predicts that the heat stored in the wall of the conductivity cell manufactured by Sea-Bird Electronics (SBE) produces a detectable error in the measured conductivity. This error is characterized by an initial magnitude of the fluid thermal anomaly, $\alpha = 0.043$ and a relaxation time of 4.3 s. This estimate does not account for the heat stored in the epoxy coating around the cell which could prolong considerably the relaxation time of the cell. This is a companion contribution to RGL that tests his theoretical predictions with oceanic data collected in a thermohaline staircase.

As discussed in RGL, three factors characterize the response of a conductivity cell: (i) the initial flushing of the interior of the cell, (ii) the boundary layer on the wall of the cell and (iii) the heat stored in the wall of the cell. Here we will refer to the response governed by flushing and by boundary layer diffusion as the "short-term" response while that part regulated by the heat stored in the wall will be denoted the "long-term" response because the time scale of (iii) is one order of magnitude larger than the scales of (i) and (ii). Our focus will be on the long-term response of the SBE conductivity cell and, to reach that goal, we also deal with the short-term response of this cell.

We first noticed the effect of the thermal inertia of the conductivity cell in the computation of salinity and potential density with data collected in the C-SALT Experiment (Schmitt et al. 1987), where the gradients of salinity and temperature are aligned and make almost equal and opposite contributions to the gradient of potential density. Between 300 and 600 m depth, the vertical profiles of salinity and temperature have the form of a staircase—mixed layers 10 to 20 m thick separated by interfaces 0.5 to 3 m thick (Fig. 3). This staircase-like structure offers a nearly ideal environment for examining the short- and long-term responses of a conductivity cell. However, the hardware configuration used in the experiment was not optimal for examining the short-term response. Vertical profiles of the computed potential density show inversions, with 8 m vertical scales, in the tops of the mixed layers that cannot be real in view of the low levels of turbulence found in this thermohaline staircase (Lueck 1987; Gregg and Sanford 1987). Density errors were detectable for 45 s after entering a mixed layer.

The next section provides a background on the instrumentation, presents some representative data from the thermohaline staircase and shows how we minimized the short-term mismatch between the conductivity cell and the thermometer so that the remaining errors stem mainly from the thermal inertia of the cell. Section 3 gives our estimates of the two parameters of RGL's thermal model. A simple numerical algorithm is used in section 4 to produce profiles of salinity and density that are corrected for the thermal inertia of the cell, while we also investigate the speed scaling of the model parameters and the sensitivity of the computations to variations in these parameters. The last section, 5, discusses how others should use our results to correct their data. Readers wishing to see only the es-

* Also affiliated with the Department of Earth and Planetary Sciences, Johns Hopkins University.

Corresponding author address: Dr. Rolf G. Lueck, The Johns Hopkins University, Chesapeake Bay Institute, The Rotunda, Suite 315, 711 W. 40th Street, Baltimore, Maryland 21211.

sence of this contribution can do so by comparing the uncorrected profiles of salinity and density (Fig. 4) against the short-term only corrected profiles (Figs. 9 and 10) and the short- and long-term corrected profiles (Fig. 15).

2. Background

a. Instrumentation

We used a model SBE-4-01/0 conductivity probe (serial number 151) and a model SBE-3-01/F thermometer (serial number 639). These probes are standard production units, the cell had the standard 0.0032 m epoxy coating on its outer surface, and neither sensor was modified in any way. To first order, the geometry of the conductivity cell (Fig. 1, RGL) is a cylinder of inner radius 2.0×10^{-3} m, outer radius 3.95×10^{-3} m, and length 0.11 m. The outer electrodes delimit the sensitive volume of the cell. An inlet section 0.040 m long and with a radius of 3.5×10^{-3} m precedes the first electrode.

The conductivity and temperature sensors were mounted into the hull of the towed body *HOTDAD* (Lueck 1987) so that the inlet of the cell and the tip of the thermometer protruded out of the hull by 0.05 m (Fig. 1). The sensors were positioned mutually par-

allel, with the inlet of the cell 0.05 m away from the tip of the thermometer and 0.04 m higher. A strain-gauge type pressure transducer (Viatran Model 104) was mounted near the center of the towed body. Also mounted on the towed body were two velocity and two temperature microstructure sensors located right at the nose, a triaxial accelerometer positioned 0.2 m aft of the turbulence probes, a SBE pump placed near the pressure transducer and a two-axis electromagnetic current meter situated just aft of the midpoint of the body.

The SBE sensors were positioned 0.75 m aft of the nose of the towed vehicle and should have been outside of the boundary layer over the hull. At a point 0.75 m behind the leading edge of a flat plate at zero incidence and at a free stream speed of 0.85 m s^{-1} , the laminar boundary-layer thickness is 0.008 m and the turbulent boundary-layer thickness is 0.02 m (Hoerner 1965, section 2). The sensors were located in a region of increasing body diameter, where favorable pressure gradients decrease the growth of the boundary layer relative to zero pressure gradient flows and encourage its attachment to the hull. On the other hand, the two sharp circular edges on the pressure case near the nose of the body will encourage flow separation and a transition from laminar to turbulent flow in the boundary

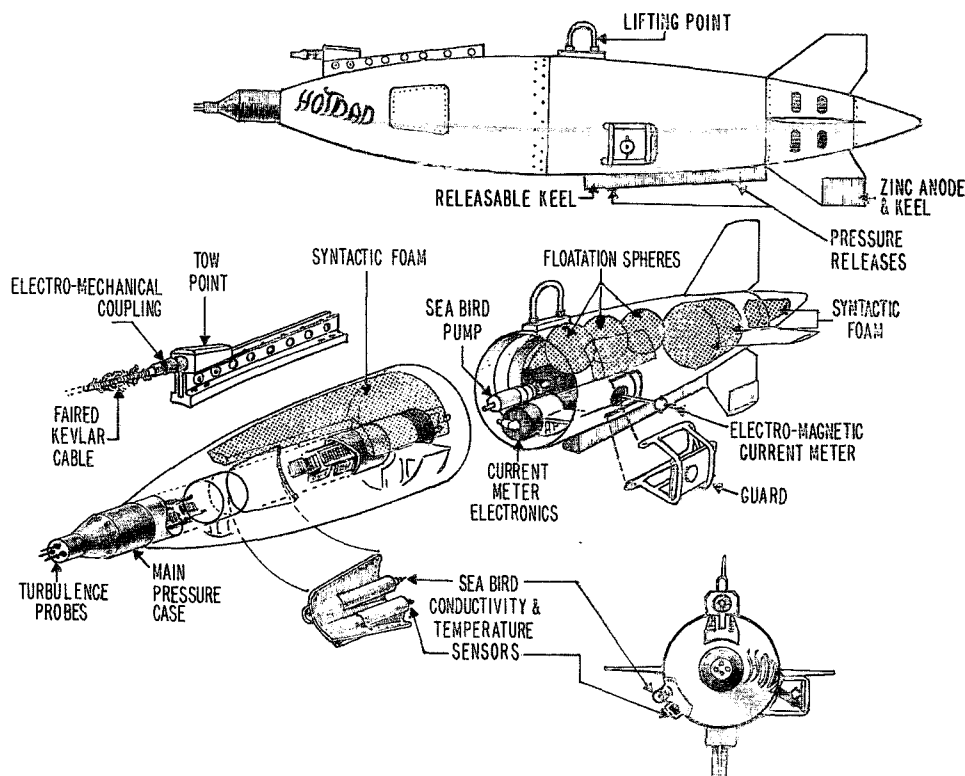


FIG. 1. A sketch of the towed body *HOTDAD* showing the mounting position of the conductivity and temperature sensors on the starboard side and 0.75 m aft of the turbulence probes. The thermometer is 0.05 m away and 0.04 m below the conductivity cell. The body is 3.8 m long and 0.61 m wide at its midsection.

layer. Even if the boundary layer were turbulent, the sensors should have been outside of it, and even if they were not, thermal effects from the hull would have influenced both sensors equally.

The data reported here were collected at tow speeds of 0.85 m s^{-1} and 1.8 m s^{-1} . Our tow speeds are similar to those of other instruments (CTD, vertical profilers, etc.). Flow through the cell was aided by a SBE pump set to $30 \times 10^{-6} \text{ m}^3 \text{ s}^{-1}$, as recommended by the manufacturer. A tygon tube, approximately 2 meters long and with an inner diameter of 0.01 m, connected the outlet of the conductivity cell to the inlet of the pump. The wall of the tube did not collapse under the differential pressure produced by the pump. We calibrated the pumping rate of our system after the cruise by collecting the outflow in a graduated beaker over a measured time interval. For this calibration, we used the same plumbing employed during the oceanic measurements and arranged the inlet reservoir so that there was no induced static pressure across the system. For a pumping rate of $30 \times 10^{-6} \text{ m}^3 \text{ s}^{-1}$, the mean speed of the flow through the cell is 2.4 m s^{-1} (inner diameter of 0.004 m). The motion of the cell through the ocean adds a dynamic pressure at the inlet of the cell and its effect on the flow through the cell can be estimated only crudely. The flow in the cell is not fully developed pipe flow (RGL). If the actual volume flux was $30 \times 10^{-6} \text{ m}^3 \text{ s}^{-1}$ and the flow in the tygon tube was a fully developed pipe flow, the pressure drop across its length was 0.05 m (Binder 1962, Chap. 8) expressed as a head. The pressure drop across the cell was 0.25 m (Kays 1966, Chap. 6). The stagnation head at 0.85 m s^{-1} is 0.037 m, and 0.17 m at 1.8 m s^{-1} . Thus, when the cell is motionless, the pump produces a head of approximately 0.30 m. The added head of 0.037 m (0.85 m s^{-1}) would have produced a negligible flow increase because flow speed is proportional to the root of the head. The stagnation head at 1.8 m s^{-1} is about half of the pressure drop across the cell and tube at $30 \times 10^{-6} \text{ m}^3 \text{ s}^{-1}$ and should produce a significant, but less than proportional, increase in flow through the cell. Thus, at a tow speed of 0.85 m s^{-1} , the flow through the cell is very likely close to 2.4 m s^{-1} while at a tow speed of 1.8 m s^{-1} , the flow speed is larger, but not proportionally so. These estimates are crude because we have ignored diameter transitions in the cell and at the junction between the cell and the tygon tube, and we have also neglected flow accelerations around the towed body. We are unaware of any attempt to measure the rate of flow through the cell while it is moving.

The conductivity, temperature and pressure signals were sampled 64 times per second. The frequency output from the SBE sensors was determined by a period-counting technique. A precision 10 MHz clock was counted for 72 cycles of the signal. The count is proportional to the period of the output signal from the SBE sensors and, for typical conditions, is a 17-bit

number. The most significant bit was dropped and the remaining 16 bits were recorded. The missing 17th bit is easily restored if the temperature is known to within 20°C . The least count is approximately $3 \times 10^{-4}^\circ\text{C}$ and $5 \times 10^{-5} \text{ S m}^{-1}$ ($1 \text{ S m}^{-1} = 10 \text{ m}\Omega^{-1} \text{ cm}^{-1}$). The analog voltages produced by the pressure circuit and its time-derivative were transformed into 15-bit numbers with an A/D converter. The bit resolution of the pressure signal is 0.04 db (1db = 10^4 pascals). We combined the pressure and the rate-of-change of pressure signals to produce a synthetic pressure record with a resolution that is better than 1×10^{-3} db. The synthetic pressure record allows us to plot signals against depth without producing spurious vertical displacements because of the limited resolution of the original pressure record.

The conductivity sensor was calibrated on 1-18-85, used in November 1985 and recalibrated on 5-23-86. In the range of 3 to 4 S m^{-1} , the cell drifted by 0.002 S m^{-1} . The temperature sensor was calibrated on 3-18-85 and 5-16-86 and drifted 0.008°C between 10° and 15°C . We used the post-cruise calibrations to convert the signals to physical units. The drift of the calibration coefficients and absolute errors in the measured conductivity and temperature have negligible effects on the results reported here—they produce, at most, a uniform offset. The conductivity cell has a pressure coefficient of approximately 10^{-7} per db, too small to warrant inclusion in our computations. The pressure transducer was calibrated before and after the cruise with a dead-weight tester that had, one year earlier, been checked with a quartz-pressure transducer. The accuracy of the pressure calibration is 0.1%, there was no change from the pre- to the post-cruise calibration, and the hysteresis of the transducer over a pressure change of 600 db is less than 1 db.

Although much of the data that we will show is plotted as a vertical profile, the path of the body is neither vertical nor horizontal. The bulk of our analysis comes from a section where the towed body descended fairly smoothly at a rate of 0.17 m s^{-1} while its mean speed was 0.85 m s^{-1} (Fig. 2). Thus, the path was declined 12° below horizontal and one meter of vertical distance corresponds to 5 meters of horizontal travel. It was our initial hope that such a profile would provide a much higher resolution of the hydrographic characteristics than would a vertical profile. For the purpose of plotting only, we take the depth in meters to be identical to the pressure in decibars and thereby cleave to the MKS system without expressing pressure in units of pascals.

b. Data

Our data were collected in the tropical North Atlantic ($12^\circ 06' \text{N}$, $56^\circ 30' \text{W}$) 320 km east of Barbados where the thermocline takes the form of a well-developed staircase (Fig. 3). Between the depths of 300 and 600 m, the density ratio

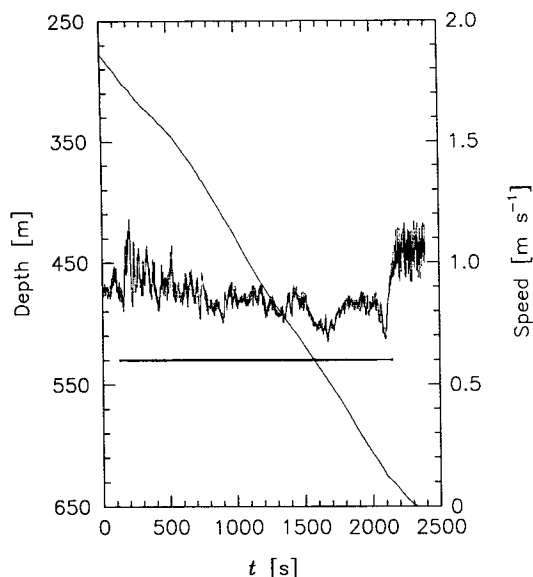


FIG. 2. The time profile of the speed and the depth of the towed body on its initial descent. The horizontal bar marks the range used to compute the transfer function of the cell relative to the thermometer.

$$R_\rho = \frac{\alpha' \left. \frac{\partial \rho}{\partial T} \right|_{S,P}}{\beta' \left. \frac{\partial \rho}{\partial S} \right|_{T,P}} \quad (1)$$

where α' is the thermal coefficient of expansion and β' the saline coefficient of contraction, is fairly uniform and near 1.5. (The coefficients α' and β' should not be confused with α and β in RGL's thermal model.) With salinity changes almost proportional to temperature fluctuations, the conductivity signal is very nearly proportional to temperature. This factor aids the determination of the relative response of the sensors. At a density ratio of $R_\rho = 1.5$, sixty-seven percent of the density changes induced by temperature are compensated by salinity changes, making the computation of density very sensitive to errors in the measured conductivity. At $R_\rho = 1.5$, 86% of the conductivity signal is induced by temperature, while 14% is caused by salinity and a small, but significant, amount comes from pressure.

We used the algorithms developed at the Woods Hole Oceanographic Institute (Fofonoff and Millard 1983) to compute salinity and potential density. Figure 4 shows salinity, potential temperature and potential density computed, without correction for the response of the sensors, for one of the interfaces in the staircase. While the boundary between the interface (the high gradient section) and the lower mixed layer is quite sharp in the temperature profile, the "edge" of the salinity profile is much more rounded. The computed potential density at the edge over-shoots the mixed

layer value and relaxes back its asymptotic value 8 meters below the edge. Eight meters of vertical travel corresponds to 40 meters of horizontal movement and took 45 seconds of elapsed time. The rate of dissipation of kinetic energy by turbulence was measured simultaneously from our instrument (Lueck 1987) and also by Gregg and Sanford (1987) during the course of the C-SALT experiment. The observed dissipation rates are among the lowest ever reported and are completely inconsistent with density inversions on vertical scales larger than 0.1 m. Thus, we will take as our working hypothesis that the salinity profile should mimic the temperature profile at least to the extent that density inversions are absent.

The salinity and potential density profiles (Fig. 4) show symptoms of a short-term mismatch between the thermometer and the conductivity cell—sharp spikes in salinity and density—and manifestations of a long-term mismatch—smoothing of the salinity profile and excessive density in the top eight meters of the mixed layer. Ignoring the thinnest spikes, the maximum density error is approximately 0.01 kg m^{-3} . Because there is no long-term forcing after the sensors enter the mixed layer, the error in the computed salinity and density must be due to a long-term conductivity error. There is no reason to suspect the thermometer because the edges of the temperature profile are sharp.

The long-term error is the focus of this contribution, but because the time scales of the short- and the long-term mismatches between the temperature and

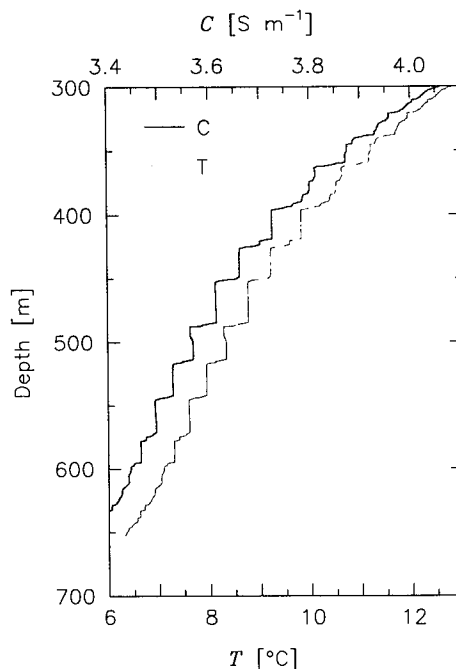


FIG. 3. Depth profile of the temperature and conductivity between 300 and 600 m measured with the SBE thermometer and conductivity cell.

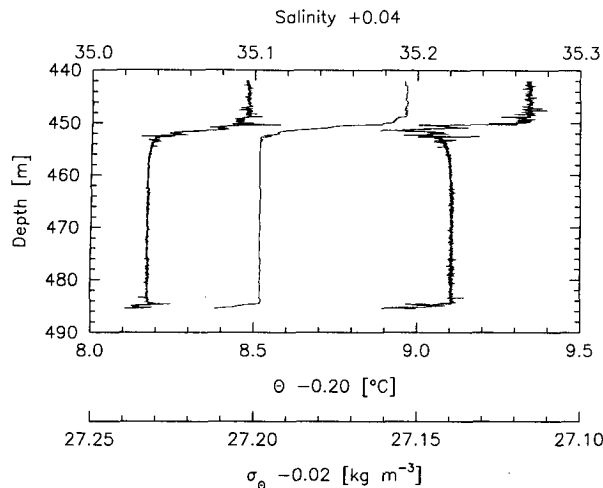


FIG. 4. Profiles of salinity (left trace), potential temperature (central trace) and potential density (right trace) with no correction applied to the temperature or the conductivity signals. The potential density scale increases from right to left so that the curves do not intersect.

conductivity sensors differ by more than an order of magnitude (RGL), these two effects can be treated independently. To highlight the long-term conductivity error, we will first adjust our signals to minimize the short-term errors.

c. Short-term mismatch

Because the short-term response of the SBE conductivity cell to temperature signals is still unknown, we used the procedure suggested by Horne and Toole (1980) to match the signals from our thermometer and conductivity cell. This strategy uses the ratio of the Fourier transforms of the in situ conductivity and temperature signals to estimate the transfer function of the cell relative to the thermometer. The assumption is that the conductivity signal is proportional to temperature fluctuations. This is a good assumption for our data because 86% of the conductivity signal was produced by temperature, and the remaining 14% due to salinity was nearly proportional to temperature because the density ratio was almost constant.

To determine the relative response of our conductivity cell and thermometer, we computed the complex transfer-function of the conductivity signal relative to the temperature signal for 64 32-second blocks of data (Fig. 5). The slope of the phase transfer-function, $(-\partial\phi/\partial\omega)$, is the lag of the conductivity signal relative to the temperature signal. The phase transfer-function has two linear regions; from 0 to 0.2 Hz, where the lag is 0.18 s, and from 0.2 to 3 Hz, where the lag is 0.077 s. (We use the word “lag” to refer to a delay in time only, which is consistent with its usage in texts on time-series filtering, but not with Horne and Toole (1980) who used the word to describe the effect of their filter, which modified both the phase and the amplitude of

their temperature data.) The lag of 0.077 s is consistent with the spatial displacement between the thermometer and the center of the cell. The output of the conductivity cell lags behind the response of the thermometer. The result of lagging the temperature by 5 samples is shown in Fig. 6. Rather than compute the optimal convolution coefficients for the inverse transfer-function, as Horne and Toole (1980) did, we will travel a simpler path. The phase and the amplitude of the transfer-function appear very similar to the combined effect of a lag of 0.077 s (5 samples) and a “lag-lead” filter given by

$$H_{ll} = (1 + s/s_T)/(1 + s/s_C), \quad (2)$$

where $s = i\omega$ is the Laplace transform variable, ω the angular frequency in radians per second, $i^2 = -1$, $s_C = 4.3 \text{ s}^{-1}$ and $s_T = 7.5 \text{ s}^{-1}$. After we lagged the temperature signal by 5 units, the lag-lead filter (2) produces a reasonable approximation of the phase transfer-function (Fig. 6). Methods for converting continuous-domain filters into discrete-domain filters are given in Antoniou (1979). A discrete filter operator equivalent to (2) is

$$T_{ll}(n) = bT_{ll}(n-1) + a_0T(n) + a_1T(n-1) \quad (3)$$

where T is the measured temperature, T_{ll} is the output of the filter and the coefficients are $a_0 = 0.5872$, $a_1 = -0.5222$ and $b = 0.9350 = 1 - a_0 - a_1$. Applying

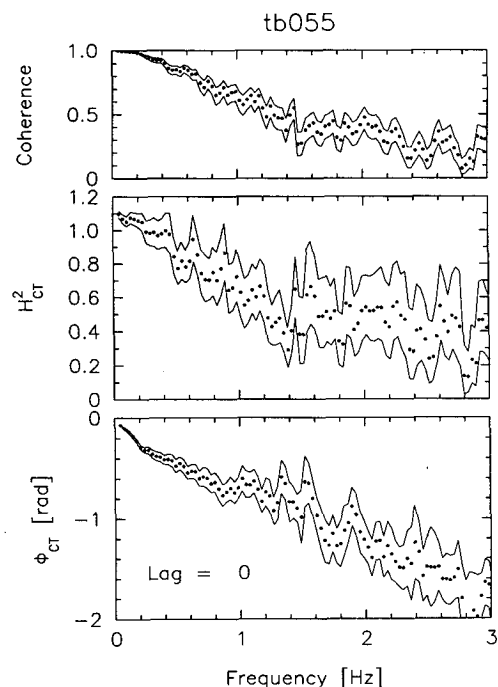


FIG. 5. The ensemble average transfer-function of conductivity relative to temperature of 64 32-second blocks of data from 280 to 640 m depth (as marked in Fig. 2). The solid lines mark the 95% confidence limits.

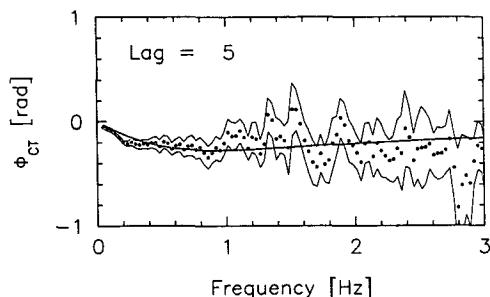


FIG. 6. Phase transfer-function after a lag of 5 units was applied to the temperature time series. The thick solid line is the phase of the lag-lead filter in Eq. (3). The power and coherence functions remain unchanged from Fig. 5.

a lag of 5 units produces the lag and lag-lead corrected temperature

$$T_{III}(n) = T_{II}(n - 5). \quad (4)$$

The filter operator in (3) and a lag of 5 units (4) were applied to the measured temperature signal, and this successfully reduced the phase difference between the conductivity and temperature signals, and flattened the amplitude response function (Fig. 7). There is, however, still some residual phase difference near 0.2 Hz.

The phase of the lag-lead filter in (2), and hence the operation in (3), is

$$\phi_H(\omega) = \tan^{-1}(\omega/s_T) - \tan^{-1}(\omega/s_C).$$

Thus, the delay of (2) and (3) is 0.10 s (6.3 units) at zero frequency, and the total lag of our operation is 0.178 s (11.3 units) at zero frequency. The lag of the lag-lead filter vanishes at high frequencies. The operation described by (3) is not a simple convolution because the output at any "time" n depends on the pre-

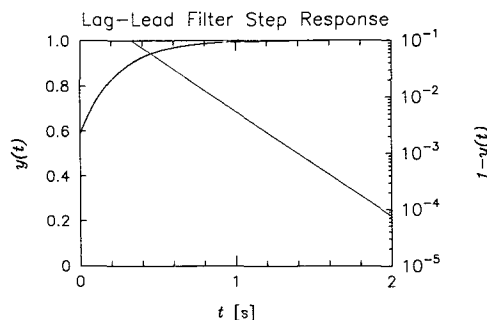


FIG. 8. Step response of the discrete realization of the lag-lead filter (3) that we applied to the temperature signal to reduce the short-term mismatch between the cell and the thermometer. Linear scale—thick line; logarithmic scale—thin and nearly straight line.

vious output as well as the current and previous inputs. The influence of the lag-lead filter lasts longer than its zero-frequency lag, and this is readily seen by applying a unit step to (3), i.e. $T(n) = 0$ for $n < 0$ and $T(n) = 1$ for $n \geq 0$. The step response (Fig. 8) differs from unity by 0.20 after 0.18 s, by 0.05 after 0.5 s, by 0.006 s after 1 second and by 8×10^{-5} after 2 seconds, at which point the influence of the filter is completely negligible.

To illustrate the short-term correction, we computed salinity with three different algorithms (Fig. 9). The first method lags the temperature by 5 units to account for the spacial displacement between the cell and the thermometer. The second method adds a correction for the relative response, i.e. the operation in (3) and (4). The third method lags the temperature by 11 units to account for the spacial displacement and (only) the zero-frequency lag of the operation in (3). All three methods reduce the spikes in the computed salinity.

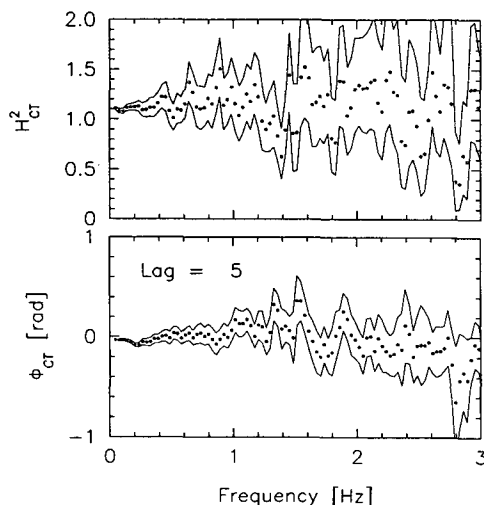


FIG. 7. The power and phase transfer-functions after the application of the lag-lead filter (3) and a lag of 5 units to the temperature time series. The coherence remains unchanged from Fig. 5.

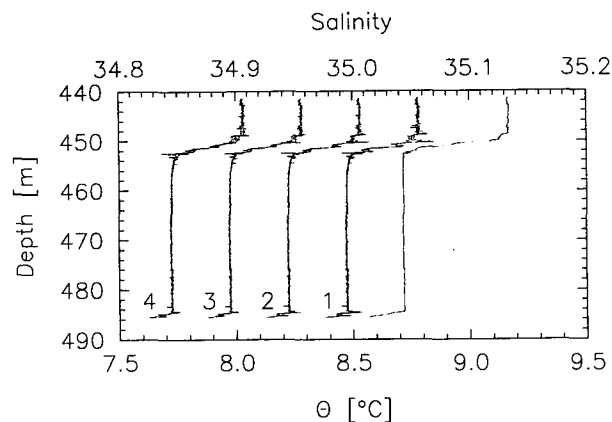


FIG. 9. Profile of potential temperature, θ , (right-most trace) and salinity after various processing of the temperature signal intended to reduce the short-term mismatch between the cell and the thermometer. The labeled salinity traces had: (1) no correction, (2) a lag of 5 units, (3) a lag of 5 units plus the lag-lead filter and (4) a lag of 11 units applied to the temperature signal.

The second method, which is the only one that has a frequency dependent phase *and* amplitude correction, reduces spiking the most. The superiority of the second method is even more obvious in the computed density (Fig. 10).

We have examined all of the interfaces measured on a descent from 300 to 650 m, and we have lagged (5 units) and lag-lead filtered (3) the temperature data from this section to minimize the effect of the short-term mismatch between the cell and the thermometer. The subsequent ascent revealed several thin interfaces and, as the speed of the towed body was then 1.8 m s⁻¹, we have used these data to test the speed scaling of RGL's thermal model (sections 3 and 5). To reduce the short-term mismatch in the data from the ascent, we used no lag and the lag-lead coefficients $s_C = 12$ s⁻¹ and $s_T = 75$ s⁻¹.

3. Estimation of model coefficients

Of the two parameters in RGL's thermal model, the time constant β^{-1} is more easily estimated. For each interface we used the measured conductivity and the short-term corrected temperature, T_{III} , to compute the salinity. We then normalized the computed salinity using

$$S(t) = S_0 + (S_1 - S_0) \cdot S_N(t) \quad (5)$$

where S_0 is the salinity in the mixed layer immediately above an interface, and S_1 is the salinity well below an interface and should represent the true salinity. Plots of $\log_e(1 - S_N)$ against time (Fig. 11) reveal a rapid decrease in the interface, followed by a nearly linear decrease for about 30 seconds before this signal becomes erratic as $S_N \rightarrow 1$. Comparison with the simultaneous temperature signal indicates that the sensor has traversed through more than 95% of the interface at the start of the linear region. A fit to the logarithmic response curve should not be made in the interface itself because, in that region, the response is forced by the input signal and is not in a freely decaying mode. For each interface, we fitted by sight a line parallel to the linear region and took its slope to be the inverse

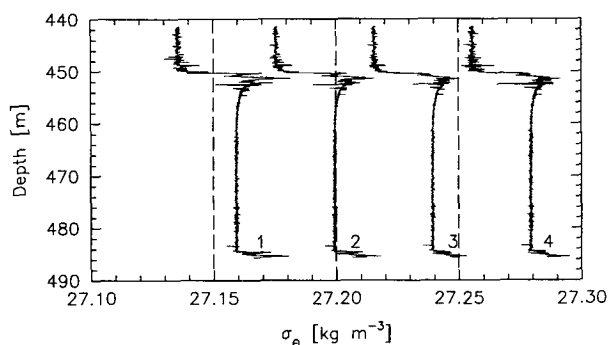


FIG. 10. As in Fig. 9, but for potential density, σ_θ .

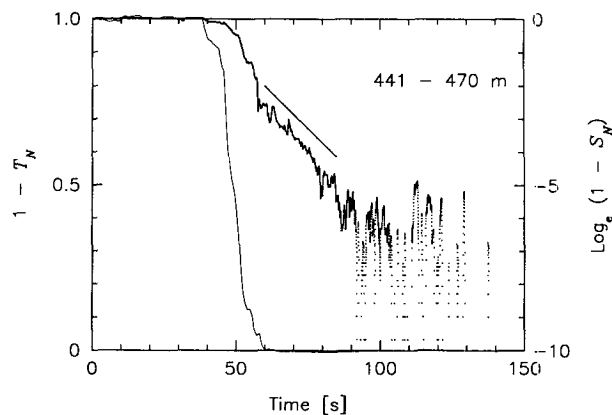


FIG. 11. Time profile of the normalized salinity, S_N , around the interface near 450 m plotted as unconnected points. The thin line is the concurrent and normalized temperature. The thick straight line is a sight-fit to the linear region of the logarithmic response.

time constant β (Table 1). The scatter of the data points in the linear region is considerable and our estimates of β have an uncertainty of nearly a factor of 2. The mean value of β is 0.10 s⁻¹ and its inverse of 10 s is about twice the value predicted by RGL. Our method requires a well-mixed layer below an interface and a sharp boundary between them, and this limits us to 8 interfaces for estimating β . We have used the computed salinity rather than the measured conductivity to estimate the decay time of the thermal anomaly because

TABLE 1. Estimates of coefficients.

Interface depth (m)	Speed (m s ⁻¹)	α	β (s ⁻¹)	Notes
345	0.88	—	0.07	1
395	0.84	—	0.08	1
424	0.86	0.03	0.10	1, 5
451	0.88	0.025	0.09	1
486	0.80	—	0.15	1
525	0.76	0.04	0.08	1
544	0.73	0.025	0.09	1
575	0.84	0.02	0.13	2
345–575	0.85	0.028	0.10	4
300–600	0.85	0.028	0.11	3
350–300	1.81	0.022	0.10	3
390–330	1.89	0.020	0.10	3
460	1.71	0.025	0.10	3
435	1.67	0.025	0.10	3
414	1.88	0.020	0.10	3

Notes:

1. Estimated using Eqs. (5) and (10).
2. The top of the mixed layer below the interface has a density stable thermohaline inversion which reduces the reliability of this estimate.
3. Estimates made by plotting potential density and varying the parameters to obtain the best fit.
4. These are the mean for the eight interfaces above this row.
5. The bottom of this interface is not very sharp.

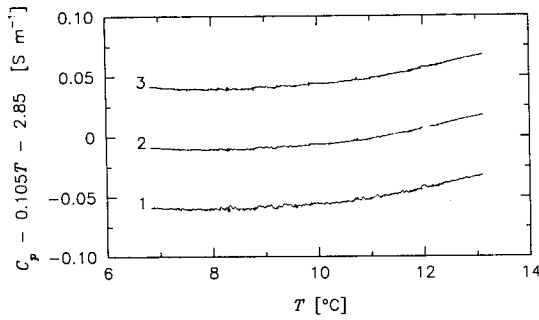


FIG. 12. The in situ conductivity corrected for the effect of pressure, C_p , less a constant (2.85) and a linear function of temperature ($0.105T$) plotted against temperature for the depth range of 280 to 640 m. The maximum deviation from a straight line is 0.01 S m^{-1} , so the pressure-corrected conductivity is linear in temperature to within 1.7%. The traces are: 1) no correction to temperature, 2) a lag of 5 units and the lag-lead filter and 3) a lag of 11 units.

salinity greatly accentuates the error and inherently removes the pressure signal from the measured conductivity.

In order to estimate α , the initial magnitude of the fluid thermal anomaly, we need to develop a linear relationship between the measured conductivity and the measured (and short-term adjusted) temperature, which requires removing the effect of pressure. We computed a "pressure-adjusted" conductivity by subtracting a linear and quadratic pressure term from the measured conductivity. Where no confusion exists, we will refer to this pseudoconductivity as simply "conductivity." Removing the effect of pressure renders the conductivity a nearly linear function of temperature (Fig. 12). The small residual curvature reflects small but systematic depth changes in the vertical gradient of salinity relative to temperature gradients. Even if the density ratio had been exactly constant, temperature dependence in the thermal coefficient of expansion would still render curvature to the CT -curve. The short-term corrected temperature has far fewer loops in CT -space than do the uncorrected and the lag only corrected temperature signals. Using the short-term corrected temperature lowers the noise in our estimates of α and β .

Let us express the measured conductivity and temperature of the fluid around an interface by

$$C(t) = C_0 + (C_1 - C_0) \cdot g(t) \quad (6)$$

and

$$T(t) = T_0 + (T_1 - T_0) \cdot f(t), \quad (7)$$

where the subscripts naught refer to conditions in the mixed layer above an interface and one refers to conditions far below an interface and should represent the true environmental conditions. The time functions g and f are the normalized signals having a value of zero

for $t < 0$ and unity as $t \rightarrow \infty$. The function $g(t) - f(t)$ is plotted for one of the interfaces in Fig. 13. This function is a little noisy and for $35 < t < 40$ it reverses sign and is therefore not monotonic as predicted, i.e. the salinity, and hence the conductivity, does not mimic the temperature. However, for the bulk of the profile it is negative as expected and has a fairly well defined extremum. The measured and normalized conductivity should be equal to the short-term corrected temperature convolved with the impulse response of the cell [RGL, Eq. (29)], which is

$$g'(t) = f(t) - \alpha f(t) + \alpha \beta \cdot \exp(-\beta t) \int_0^t f(\zeta) \times \exp(\beta \zeta) d\zeta. \quad (8)$$

For comparison against the function $g(t) - f(t)$, we also plotted in Fig. 13 the function

$$f(t) - \beta \cdot \exp(-\beta t) \int_0^t f(\zeta) \cdot \exp(\beta \zeta) d\zeta \quad (9)$$

which is much smoother and unconditionally one sided. Equation (9) should be the mirror image of $g(t) - f(t)$. We computed our integrals by a trapezoidal approximation. Knowing β , we can estimate α from the ratio of $g(t) - f(t)$ to (9), namely

$$\alpha = \{g(t) - f(t)\} \cdot \{f(t) - \beta \cdot \exp(-\beta t) \int_0^t f(\zeta) \times \exp(\beta \zeta) d\zeta\}^{-1}. \quad (10)$$

For most interfaces, (10) produces stable estimates of α for a 30 second period after the probes leave the interface (Fig. 14). As with our estimates of β , the evaluation of α is fairly subjective and our precision is not much better than a factor of 2. The mean value of α is 0.028 (Table 1), about 35% smaller than predicted by RGL.

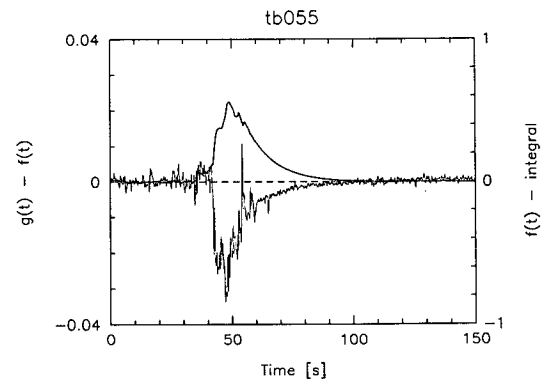


FIG. 13. The time history of the difference between the normalized conductivity $g(t)$ and temperature $f(t)$ across the interface near 450 m (thin line). The thick line is Eq. (9).

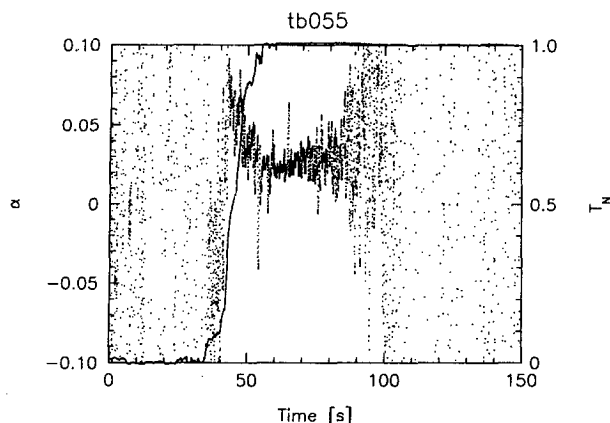


FIG. 14. The volume-weighted thermal anomaly in the conductivity cell, α , for the interface near 450 m, based on Eq. (10) and plotted as unconnected points. The solid line is the concurrent and normalized temperature.

4. Corrected profiles

a. Numerical method

In order to use our estimated coefficients (α and β) to correct the measured conductivity for the transient long-term thermal anomaly produced by the wall, we need a discrete realization of its impulse response [RGL, Eq. (27)] and must convolve this response with the short-term corrected temperature. One method would be to convert continuous time, t , into discrete time using $t = n(2f_N)^{-1}$ where n is the data index and f_N is the Nyquist frequency, which is 32 Hz for our data. Clearly, because the effect of the impulse response lasts for tens of seconds, a discrete approximation of the impulse response must include more than a thousand points, and this would make the convolution extremely inefficient. An alternative and much more efficient approach is to use the bilinear-transformation method (Antoniu 1979, section 7.6) on the Laplace-transform of the impulse response. From the frequency response [RGL, Eq. (28)] the Laplace-transform of the impulse response is

$$\Gamma(s) = \gamma s \alpha \beta^{-1} (1 + s \beta^{-1})^{-1}, \quad (11)$$

where $\gamma \approx 0.1 \text{ S m}^{-1} \text{ } ^\circ\text{C}^{-1}$ is the temperature coefficient of conductivity. The bilinear-transform method equates the Laplace variable, s , with z using

$$s = 4f_N(z - 1)/(z + 1) \quad (12)$$

to produce the transfer-function in the z -domain given by

$$\Gamma(z) = \gamma a (z - 1)/(z + b) \quad (13)$$

where $z = \exp(i\pi\Omega)$, Ω is the frequency in hertz normalized by the Nyquist frequency, and the coefficients are given by

$$a = 4f_N \alpha \beta^{-1} (1 + 4f_N \beta^{-1})^{-1} \quad (14)$$

and

$$b = 1 - 2a\alpha^{-1}. \quad (15)$$

The discrete time-domain operator is then

$$C_T(n) = -bC_T(n-1) + \gamma a [T_{III}(n) - T_{III}(n-1)] \quad (16)$$

which converts the lag and lag-lead corrected temperature T_{III} into the negative of the conductivity error induced by the thermal inertia of the cell, C_T , as discussed in RGL. The conductivity error must then be added to the measured conductivity to produce a long-term corrected signal, i.e.

$$C_h(n) = C(n) + C_T(n). \quad (17)$$

Strictly, we should use in (16) the in situ temperature in the conductivity cell. T_{III} is probably the best estimate of this in situ temperature. The effect of the operator in (16) is equivalent to a convolution with an infinite number of terms, yet it requires only two additions and two multiplications per data point.

Readers not familiar with discrete filters may find (16) puzzling. For our Nyquist frequency a (14) is a small number (≈ 0.0280), and almost equal to α , and $-b$ (15) is close to unity (≈ 0.99844). The content of the square braces in (16) is proportional to the local temperature gradient. Thus, at any "time" n , the conductivity correction, $C_T(n)$, is almost equal to the previous correction plus a small term proportional to the local gradient of temperature. After a temperature step, the gradient vanishes and the correction decays geometrically at a rate determined by $-b$. For example, after the onset of a step of 1°C , the conductivity correction jumps to $a\gamma \approx \alpha\gamma$, and decays thereafter because of the subsequent null gradient.

In summary, our processing is the following. We use the filter-operator in (3) on the measured temperature and also lag it by 5 units (4). We denote this the lag and lag-lead corrected temperature T_{III} and use it in all hydrographic computations. We also convolve T_{III} with the operator in (16) to estimate the negative of the conductivity error C_T . The conductivity error is then added to the measured conductivity to produce the long-term corrected conductivity C_h which is used in all hydrographic computations. The results are presented below.

b. Results

The result of our long-term correction, using the parameters $\alpha = 0.028$ and $\beta = 0.11 \text{ s}^{-1}$, on the computation of salinity is shown in Fig. 15, which can be compared to the result of no correction (Fig. 4) and the effect of only a short-term correction (Figs. 9 and 10). The long-term correction sharpens the bottom of the salinity interface and brings the shape of this profile into closer agreement with the temperature profile. The over-shoot in density that spanned 8 meters vertically

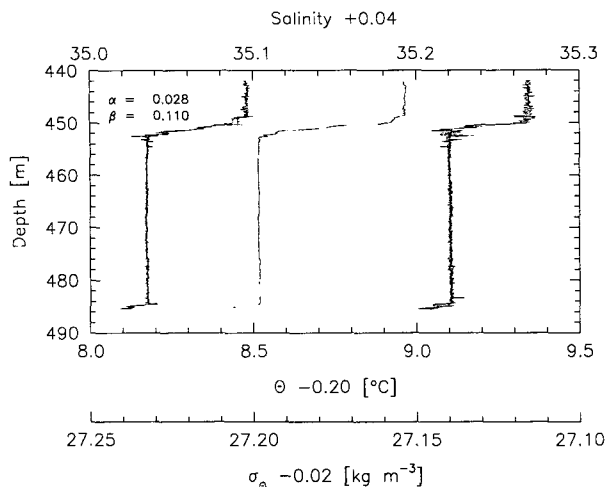


FIG. 15. Profiles of salinity (left trace), potential temperature (central trace) and potential density (right curve) with corrections for the short-term mismatch and the long-term thermal anomaly.

and had a maximum error of 0.01 kg m^{-3} (Fig. 10) has been eliminated. The only remaining error of any significance are short-term spikes in salinity and density. We have used $\beta = 0.11 \text{ s}^{-1}$ rather than the 0.1 s^{-1} , the mean from Table 1 because it appears, on very close inspection, to produce better results. However, our choice is subjective because there is little difference between the results with $\beta = 0.11 \text{ s}^{-1}$ and $\beta = 0.10 \text{ s}^{-1}$.

Smoothing the derived data with a single-pole low-pass filter set for 0.5 Hz produces results that are nearly equivalent to a box-car window that is 0.9 s wide. Thus, the effect of the filter is similar to smoothing in the vertical direction with a 0.17 m box-car window. In Fig. 15, and in all profiles before it, we have plotted every data point—64 points per second, or about 370 per vertical meter. Smoothing the data with a low-pass filter set to 0.5 Hz removes much of the noise in the salinity and density profiles (Fig. 16) and reveals some interesting structure in the interface. (We only smooth the profiles after the hydrographic computations.) For the interface near 450 m, the density interface is thinner than the temperature and salinity interface (Fig. 17)—the asymptotic density is reached at 451.4 m, whereas the salinity and temperature reach their mixed layer values at 452.7 m. The density inversions with sub-meter scales near the top of the mixed layer occur where there are still significant gradients in temperature and salinity—temperature and salinity compensate completely in terms of density, and hence, the density ratio is 1. A similar, but less pronounced, feature is evident near the top of the interface at 449.0 m where the gradients of temperature and salinity have no concurrent density gradient. This feature is not an artifact of our data processing, because the position and thickness of the salinity, temperature and density interfaces concur

for six of the eight interfaces (e.g., Fig. 18). In the seventh interface the density gradient vanishes 0.4 m above the temperature and salinity mixed layer.

The two close up views of the interfaces (Figs. 17 and 18) reveal numerous submeter scale salinity and density inversions. The density inversions correlate well with the salinity inversions and typically have a vertical scale of 0.4 m. Except for some ripple between 452 and 453 m, the temperature profile is much smoother than either the density or the salinity profiles. Because the scale of the inversions is inconsistent with the constraints imposed by the turbulence measurements and because the temperature profile is comparatively smooth, the residual density inversions represent either remnant errors in conductivity due to incomplete matching of the temperature response of the cell to the thermometer, or errors due to the salinity response of the cell, or problems associated with the vertical separation of the thermometer and the cell, or any combination of these.

The shape of the density profiles is not excessively sensitive to variations in the parameters of RGL's thermal model. Varying the inverse time-constant β by 20% has little effect on the density profiles (Fig. 19), while variations of a factor of 2 produce noticeable, but not dramatic, changes. Similar results are produced by varying α , except that a two fold increase from 0.028 to 0.056 produces an unrealistic amount of correction (Fig. 20). Other users of the SBE cell that do not run their pumps at $30 \times 10^{-6} \text{ m}^3 \text{ s}^{-1}$ should be able to scale our estimates without producing unrealistic profiles because of small errors in α or β . Even when the parameters, α and β , are in error by a factor of 2, the algorithm still produces profiles that are superior to uncorrected ones.

Figure 21 shows, for the entire thermohaline staircase, the potential density computed with (i) the combined short- and long-term corrections, (ii) only the

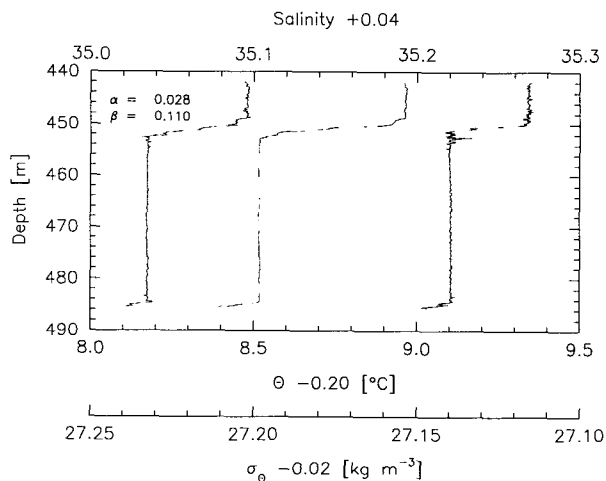


FIG. 16. As in Fig. 15, but smoothed with a 0.5 Hz low-pass filter.

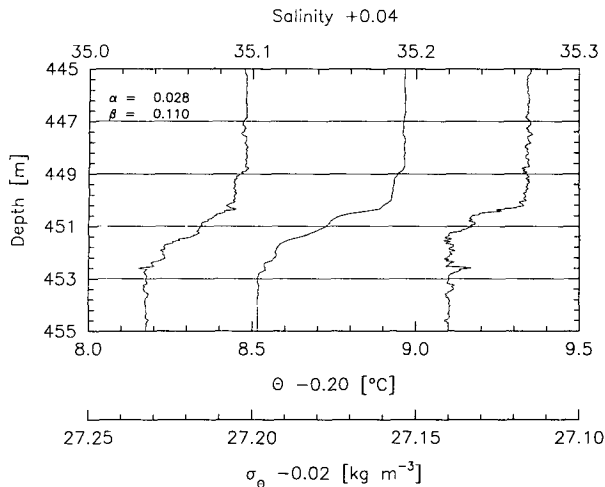


FIG. 17. Close up view of the interface near 450 m showing that the density interface (right trace) is thinner than the salinity (left trace) and temperature (central trace) interfaces. The profiles were smoothed with a 0.5 Hz low-pass filter.

short-term correction and (iii) no correction. Our algorithm removes the density inversions from the tops of all of the mixed layers. A close inspection of the profile (Fig. 21) shows that not all of the layers are completely mixed in density. A relatively thin layer near 345 m appears well mixed in the uncorrected profiles while a gradient is revealed in the corrected profile.

Figure 22 shows uncorrected profiles through three interfaces observed on an ascend while the towed body was travelling approximately 1.8 m s^{-1} and climbing 0.24 m s^{-1} (7.6°). The interface near 331 m is 0.5 m thick. An upward profile produces negative density anomalies on the upper side of the interfaces. The model parameters that produce the best results (Fig.

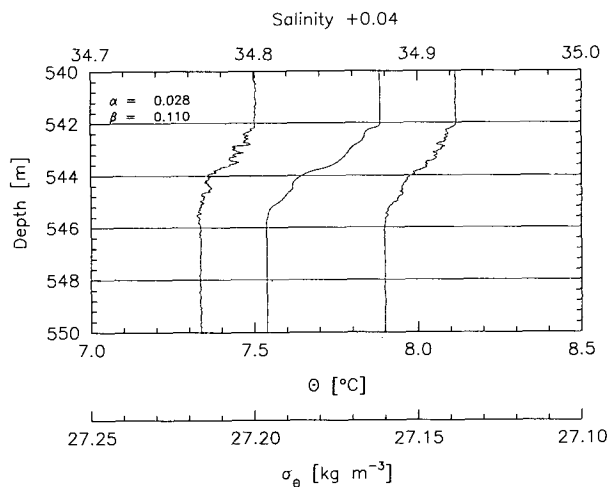


FIG. 18. Close up view of the interface near 544 m showing that the density (left trace), temperature (central trace) and salinity (right trace) interfaces coincide in depth and thickness. The profiles were smoothed with a 0.5 Hz low-pass filter.

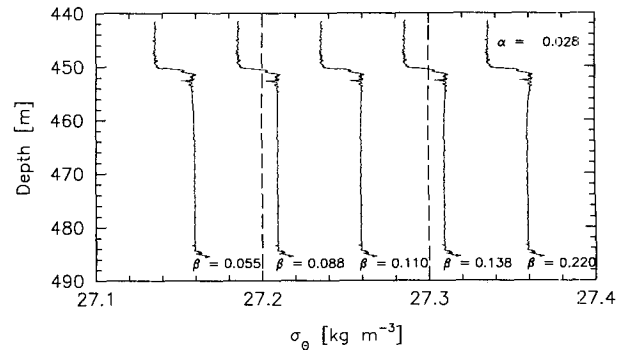


FIG. 19. Sensitivity of the computed potential density to variations in the inverse time-constant β .

23) are $\alpha = 0.020$ and $\beta = 0.10$. Larger values of β leave an unstable trend in the density profiles that is only noticeable in a very close inspection. Table 1 summarizes the model parameters that produce the best fit for all of the interfaces.

The value of β that produces the best fit is essentially the same for the high and the low speed tows, and this is consistent with the speed scaling predicted by RGL. The best value of α decreases significantly with increasing tow speed. The decrease should have been proportional to the tow speed, but because our cell was pumped, the actual flow speed through the cell is ambiguous. As discussed in section 2a, we can be certain that the flow through the cell will increase with increasing tow speed, but not by a proportional amount. Thus, the values of α are qualitatively consistent with the scaling predicted by RGL, but a quantitative assessment of the speed scaling requires a better knowledge of the actual flow through the cell than is currently available.

5. Discussion

How should others use our algorithm to correct for the thermal inertia of the SBE conductivity cell? Fortunately, the results of our algorithm are not overly

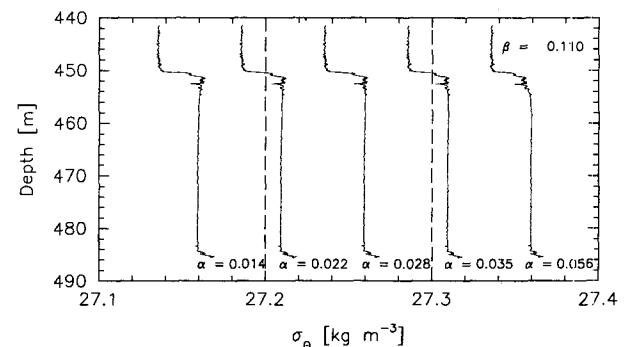


FIG. 20. Sensitivity of the computed potential density to variations in the initial value of the thermal anomaly, α .

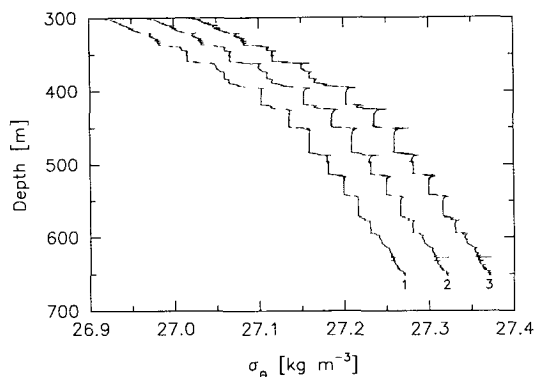


FIG. 21. Potential density for the entire thermohaline staircase. The traces are: (1) short- and long-term corrected, (2) only short-term corrected and displaced 0.05 units towards the right and (3) uncorrected and displaced 0.1 units towards the right. All profiles were smoothed with a 0.5 Hz low-pass filter.

sensitive to errors in its two parameters α and β . RGL predicted that the relaxation time, β^{-1} , is not very sensitive to flow speed, nor to conditions—laminar versus turbulent flow—inside the cell. This insensitivity is born out by our results for tow speeds of 0.85 and 1.8 m s^{-1} . Ignoring the heat stored in the epoxy coating, RGL predicted $\beta = 0.23 \text{ s}^{-1}$. However, the heat stored in the epoxy exceeds considerably the heat stored in the glass, and the relaxation time for this component alone was estimated to be 15.8 s ($\beta = 0.06 \text{ s}^{-1}$). Less than half of the heat stored in the epoxy reaches the fluid flowing through the cell. Thus, the effect of the epoxy on the relaxation time of the measured conductivity is unclear, and the estimate of $\beta = 0.23 \text{ s}^{-1}$ by RGL is an upper limit. Other users of epoxy coated SBE cells should use $\beta = 0.10 \text{ s}^{-1}$ for their corrections.

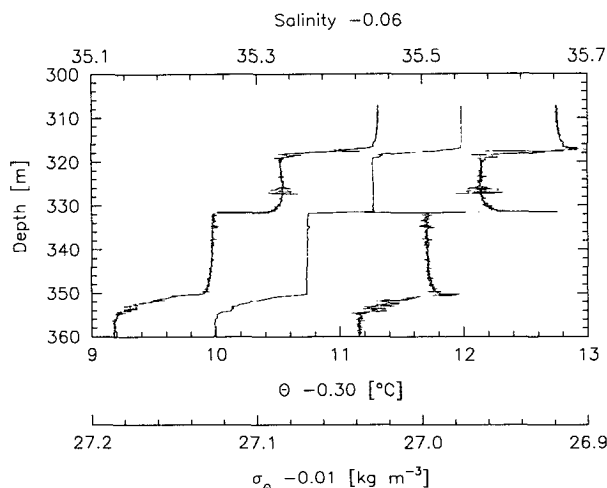


FIG. 22. The profiles of salinity (left trace), potential temperature (central trace) and potential density (right trace) with no short- or long-term correction to the conductivity or the temperature from an ascent while the towed body was travelling 1.8 m s^{-1} .

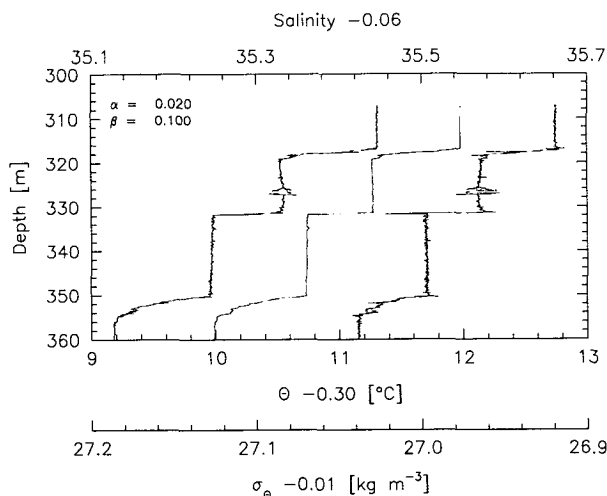


FIG. 23. As in Fig. 22, but corrected for the short-term mismatch and the long-term thermal anomaly.

Our estimate of α is 35% smaller than predicted by RGL, and this is puzzling because any heat contributed by the epoxy should increase α . There are several possible explanations because α is sensitive to conditions in the fluid passing through the cell. Our estimate of the flow speed could be too low by 35% ($\alpha \propto u^{-1}$). The flow could be turbulent aft of the central electrode because of the expansion and contraction at this electrode. Flow acceleration is more important than assumed by RGL. All of these factors reduce α and leave β essentially unchanged (RGL, Table 2). Thus, we recommend $\alpha = 0.028$ if the cell is pumped at $30 \times 10^{-6} \text{ m}^3 \text{ s}^{-1}$, and a scaling with u^{-1} for other rates, if the flow into the cell is not ducted.

Motivated by a preprint of this contribution, SBE has examined data collected (by others) with the SBE cell for evidence of thermal contamination (Larson, personal communication 1990). Values of α and β were chosen to minimize differences between the TS -curves from down and up profiles. The data were collected with the SBE duct mounted on the inlet of the cell and the plumbing was arranged to make the flow through the cell independent of the profiling speed and the direction of the profile. The pumping rate was $30 \times 10^{-6} \text{ m}^3 \text{ s}^{-1}$. Optimal results were obtained for $\beta = 0.1$ (as found by us), but α was 0.015 to 0.020 (nearly half the value found by us). The duct is almost certainly going to generate a turbulent flow in the cell, and RGL predicted a halving of α for turbulent flow at a fixed pumping rate. Thus, the results by SBE and us are qualitatively consistent with the thermal model developed by RGL, but the numerical values of the parameters α and β are different because of complications with real flows through the cell and its epoxy coating that go beyond the scope of RGL's model. Because the results of the corrective algorithm are not overly sensitive to the choice of α and β , any reasonable estimate

of these parameters will improve the salinity and density profiles. For example, a factor of two error in the coefficients is still better than no correction (Figs. 19 and 20). Users can test and tune their choice of α and β by comparing up and down traces in TS -space and, if the data are available, by examining the salinity and density profiles near sharp interfaces.

One of the weaknesses of this study is the ambiguity concerning the rate of flow through the cell at a tow speed of 1.8 m s^{-1} . With the benefit of hindsight, we support the latest recommendations on pump plumbing by SBE. The outlet from the pump should be routed so that it faces into the flow, where the speed is comparable to the flow impinging on the inlet of the cell. This arrangement will cancel the induced dynamic pressure and, with some care in the layout of the tubing, will reduce significantly flow fluctuations induced by inertial accelerations.

There is evidence that the conductivity reported by other cells is also compromised by the heat stored in the wall. Vertical profiles taken with an NBIS system by Gregg and Sanford (1987) concurrently with our towed body measurements also show density inversions in the tops of the mixed layers. Inversions are clearly evident in their Figs. 1 and 3, and it appears that they span less than 2 m. Their vertical profiler fell at 0.25 m s^{-1} , so the density error was detectable for less than 4 s. Their profiles are analogous to ours taken on a descent. For a flow rate of 0.25 m s^{-1} through an NBIS cell, RGL predicted $\alpha = 0.24$ and $\beta^{-1} = 2.2 \text{ s}$, and for these values the error is detectable for 2 s if the conductivity resolution is equivalent to 0.001°C . Thus, measurements with an NBIS cell also suffer from the heat stored in the wall, but the values cited here should be interpreted qualitatively because we are unfamiliar with the data processing used by Gregg and Sanford (1987).

6. Conclusions

The thermal inertia of the wall in the SBE conductivity cell produces a volume-weighted thermal anomaly in the sensitive section of this cell with an initial value of 2.8% and a relaxation time of 9 to 10 seconds when the mean flow through this cell is 2.4 m s^{-1} . The cell examined had a standard epoxy coating and its inlet was not ducted. After traversing through a sharp interface with a temperature contrast of 0.6°C , the heat stored in the wall induces an error in the computed

density that has an initial magnitude of 0.01 kg m^{-3} and remains detectable for 45 s. The relaxation time of the thermal anomaly of the fluid travelling through the SBE cell is twice the value predicted by RGL, while its initial value is 35% lower than anticipated. The increased relaxation time is probably caused by the heat stored in the epoxy coating. The predicted speed scaling of the initial value and relaxation time of the thermal anomaly are only qualitatively confirmed owing to some ambiguity in the actual flow speed through the cell.

We have developed an efficient numerical algorithm that uses the measured temperature to remove the conductivity error produced by the thermal anomaly. Although the error produced by the thermal anomaly is very large, in the computed salinity and density, the algorithm removes these errors almost completely. The results of this corrective algorithm are not overly sensitive to the value of its two coefficients. A misjudgment of as much as a factor of 2 in the value of the coefficients still results in profiles that are superior to uncorrected profiles.

Acknowledgments. Helpful discussions were held with N. Larson of Sea-Bird Electronics and T. Osborn. The detailed comments by one of the reviewers were extremely useful. This work was supported by the National Science Foundation under Grant OCE-8716410.

REFERENCES

- Antoniou, A., 1979: *Digital Filters: Analysis and Design*. McGraw-Hill, 524 pp.
- Binder, R. C., 1962: *Fluid Mechanics*. 4th ed., Prentice-Hall, 453 pp.
- Fofonoff, N. P., and R. C. Millard, 1983: Algorithms for computation of fundamental properties of seawater. UNESCO Tech. Pap. in Mar. Sci., No. 44, 53 pp.
- Gregg, M. C., and T. B. Sanford, 1987: Shear and turbulence in thermohaline staircases. *Deep-Sea Res.*, **34**, 1689–1696.
- Hoerner, S. F., 1965: *Fluid-Dynamic Drag*. [Published by the author, PO Box 342, Brick Town, N.J. 08723.]
- Horne, E. P., and J. M. Toole, 1980: Sensor response mismatches and lag correction techniques for temperature-salinity profilers. *J. Phys. Oceanogr.*, **10**, 1122–1130.
- Kays, W. M., 1966: *Convective Heat and Mass Transfer*. McGraw-Hill, 387 pp.
- Lueck, R. G., 1987: Microstructure measurements in a thermohaline staircase. *Deep-Sea Res.*, **34**, 1677–1688.
- , 1990: Thermal inertia of conductivity cells: Theory. *J. Atmos. Oceanic Technol.*, **7**, 741–755.
- Schmitt, R. W., H. Perkins, J. D. Boyd and M. C. Stalcup, 1987: C-SALT: an investigation of the thermohaline staircase in the western tropical North Atlantic. *Deep-Sea Res.*, **34**, 1655–1665.